J. Vis. Commun. Image R. 24 (2013) 1414–1430

Contents lists available at ScienceDirect

J. Vis. Commun. Image R.

journal homepage: www.elsevier.com/locate/jvci

Multi-feature gradient vector flow snakes for adaptive segmentation of the ultrasound images of breast cancer

Annupan Rodtook [a], Stanislav S. Makhanov [b,*]

[a] Department of Computer Science, Ramkhamhaeng University, Bangkok 10240, Thailand
[b] School of Information and Computer Technology, Sirindhorn International Institute of Technology, Thammasat University, Pathum Thani 12000, Thailand

ARTICLE INFO

Article history:
Received 3 December 2012
Accepted 21 September 2013
Available online 4 October 2013

Keywords:
Active contours
Breast cancer
Ultra sound images
Direction score
Convergence
Numerical experiments
Ground truth
Ultrasound images of breast cancer

ABSTRACT

Segmentation of ultrasound (US) images of breast cancer is one of the most challenging problems of the modern medical image processing. A number of popular codes for US segmentation are based on a generalized gradient vector flow (GGVF) method proposed by Xu and Prince. The GGVF equations include a smoothing term (diffusion) applied to regions of small gradients of the edge map and a stopping term to fix and extend large gradients appearing at the boundary of the object.

The paper proposes two new directions. The first component is diffusion as a polynomial function of the intensity of the edge map. The second component is the orientation score of the vector field. The new features are integrated into the GGVF equations in the smoothing and the stopping term.

The algorithms, having been tested by a set of ground truth images, show that the proposed techniques lead to a better convergence and better segmentation accuracy with the reference to conventional GGVF snakes. The adaptive multi-feature snake does not require any hand-tuning. However, it is as efficient as the standard GGVF with the parameters selected by the "brutal force approach". Finally, proposed approach has been tested against recent modifications of GGVF, i.e. the Poisson gradient vector flow, the mixed noise vector flow and the convolution vector flow. The numerical tests employing 195 synthetic and 48 real ultrasound images show a tangible improvement in the accuracy of segmentation.

1. Introduction

The accuracy of the computer based diagnostics of the ultrasound images of breast is still not sufficient especially in early stages when the cancers are very subtle and vary in appearance. Moreover, it is often difficult to separate the tumor from the background even when its existence is evident. Therefore, segmentation of tumors is one of the most important problems in the computer aided US diagnostics of breast cancer.

Among the most promising techniques for extraction of complex objects from digital images are active contours or snakes, originally introduced by Kass et al. [1]. Since the seminal work of Kass and colleagues, techniques based on active contours have been applied to many object extraction tasks with a different degree of success.

In particular, snakes have been used to locate the objects in various applications of medical image processing such as segmentation of abnormalities in the images of the human heart, liver, brain, breast [2–10]. The main drawback of the method is that the noise and small objects may attract the snake to a local energy minimum, which does not correspond to the actual boundary. Therefore, to reach the desired boundary, the initial contour should be initialized close to the object. The most important component of the snake based segmentation is an external force which pushes the snake towards the object. This force is usually derived from the gradient of the image gray level. Therefore, in order to enhance the effect of the external force the gradient created nearby the boundary must be extended so that the snake "feels" the object even if it is initialized far from it.

A popular solution is the balloon snake where such a force is generated artificially. This works for both contracting and growing snakes (balloons or artificially inflated contours) proposed in [11]. The distance snakes [12] exploit a similar idea. The external force is constructed as the negative of the external energy gradient, which is the distance from each point to its closest edge points in the image. Consequently, the initial contour can be located far away from the desired boundary if there are no spurious edges along the way. Furthermore, many variations of this idea such as the "stop and go" snakes [13], multi-direction snakes [14], gravitation force snakes [15], watershed-balloon snakes [16], balloon snakes with nonlinear filtering [17] have been introduced and analyzed. The image force is modified or altered to increase the capture range and decrease the sensitivity to a possible noise, shadows and (in case of the medical images) obstructing structures and tissues.

* Corresponding author.
E-mail address: makhanov@siit.tu.ac.th (S.S. Makhanov).

1047-3203/$ - see front matter © 2013 Elsevier Inc. All rights reserved.
http://dx.doi.org/10.1016/j.jvcir.2013.09.009

Another group of methods is based on minimization of the energy subject to a certain conditions improving the convergence and accuracy. Sectored snakes [18] deform the contour subject to constraints derived from a priori knowledge of the object shape, extracted from the training set of images. Fourier type descriptors have been used in [19] to evolve the curve to a prescribed shape defined by a template. The prior information is introduced through a set of invariants (translation, rotation and scaling) computed using the Fourier Transform. Furthermore, the force includes not only the edge based features but region based features as well. For instance, the homogeneity of the enclosed region [20,21]. In [22] region-based image features are combined with the edge-based features incorporated in the external forces.

Starting from multiple seeds, [22] performs segmentation of the entire image by iterative boundary deformation and region merging iteratively.

The so-called T-snakes proposed in [23] and their improvements such as the dual T-snakes [24] based on iterative re-parameterization of the original contour are able to make the use of the self loops. However, the approach allows only "rigid" deformations limited by the superimposed "simplicial grid". An intrinsic internal force that does not depend on contour parameterization based on regularized contour curvature profile has been proposed in [25,26].

A competing approach called the level set method (LSM) [27] is based on the ideas proposed by Osher and Sethian [28] to use a model of propagating liquid interfaces with curvature-dependent speeds. The LSM combined with the contour energy minimization resulted in a variety of the so-called geodesic deformable models [29–32]. However, the LSM makes it difficult to impose arbitrary geometric or topological constraints on the evolving contour via the higher dimensional hyper surface. Besides, the level set models may generate shapes having inconsistent topology with respect to the actual object, when applied to noisy images characterized by large boundary gaps [33] and non-closed curves [34].

Another group of competing approaches includes region based models aiming to smooth the image within the homogeneous regions but not across the boundaries of such regions. One of the most popular and widely studied is the Mumford and Shah model [79]. The original Mumford–Shah functional consists of a fidelity term, forcing the solution to be as close as possible to the given image, a smoothing term forcing the solution to be as smooth as possible everywhere except the image discontinuities and the geometric term, forcing the total length of the edges to be as short as possible. A variety of the Mumford–Shah model has been proposed and analyzed (see a survey [80]). One of the most significant developments is the Chan–Vese model [81] which is a level set implementation of the piecewise constant case of the Mumford–Shah model. Recent combinations of the Mumford–Shah techniques and active contours include active contours without edges [82], splitting active contours [83] and Mumford–Shah shape-prior active contours [84].

Rochery et al. propose a parametric model for higher-order active contours, in particular, quadratic snakes, for extraction of linear structures like roads [35]. The idea is to use a quadratic formulation of the contour's geometric energy to encourage anti-parallel tangents on opposite sides of a road and parallel tangents along the same side of a road. These priors increase the final contour's robustness to partial occlusions, decrease the likelihood of false detections in regions not shaped like roads, and help to prevent self-looping.

Further improvements lie along the lines of processing the underlying vector field rather than modifying the snake model itself. A number of popular codes are based on a gradient vector flow (GVF) method proposed by Xu and Prince [36,37]. A "raw" gradient vector field derived from the image edges is replaced by a vector field which minimizes a certain variational functional. The functional is designed to extend the large gradients far from the boundary, smooth the noise and speckles while keeping gradients attached to strong edges.

The generalized gradient vector flow field (GGVF) [38] extends the GVF method by introducing non-uniform diffusion. The GGVF is defined as a steady state solution of a system of parabolic equations with the elliptic terms and the source term similar to the GVF model. However, the GGVF employs space-dependent diffusion which provides better segmentation accuracy and a larger capture range. Some variations of these ideas are the multidirectional GGVF based on a special algorithm to evaluate the gradients and the diffusion coefficients [14] and the non-linear diffusion method presented in [39].

Numerous research papers apply the GGVF based active contours to medical images. The examples are multi-direction snakes: skin cancer images [14], topology-adaptive snakes: MR brain images and CT scans[23], gravitational force snakes: a variety of medical and non-medical images [15], narrow-band snakes: MRI and CT scan images of lungs [40], distance snake, GVF snake, balloon snake, "area and length" snakes, geodesic snakes, constrained snakes and level set method: MRI, CT and US images of brain, liver, kidney [32], region-competition snakes (originally [22]): CT scan slices of arteries [41], sectored snakes: abdominal CT scans[5], parametric snakes: US of breast masses [42], 3D-snakes: US breast cancer images [42,43], GVF snakes with edge map pre-processing: US of the kidney tumors [9], GVF snakes combined with the region growing and the median filter: US breast tumors [10], sketch-snakes: chest X-ray images [43], combination of snakes and active shape models: US of the human heart [44], the so-called early-vision and the discrete-snake model: a variety of the US images [47], multi-resolution snake: echographic and echobrachial images [48], GGVF snakes combined with a continuous force field analysis: breast tumor US images [49].

The success of such segmentations critically depends on preprocessing. As a matter of fact, it is often more important than selecting and tuning the active contour. The Gaussian, mean and median filters [50], Gabor filters [47] and speckle noise filters [50–53] are among the most popular for the US imagery. A fusion of the median and the Wiener filter combined with a contrast adjustment technique and the Frost speckle filter [52] is applied in [54]. A tree-structured nonlinear filter and special types of wavelet transforms has been proposed for transrectal ultrasound [55]. The active contour is used by the segmentation module. A comparison between the segmented image with and without the preprocessing shows that this module provides an improvement in the accuracy of the boundary detection. A combination of filtering, edge map and initialization by a human operator [10] employs an iterative truncated median filter to reduce the speckle noise. In [56] the speckle noise is suppressed by anisotropic diffusion filter [57] and a stick filter [58].

More often than not, the preprocessing is not a single step but a well arranged sequence of operations including (but not limited to) filtering, morphological transformations and edge detection procedures specific for the particular type of medical imagery. A combination of region growing and median filtering is proposed for the GGVF snakes in [10]. A single run of the anisotropic diffusion filter (non-linear filter [59]) is proposed for the multi direction snake [14]. Non-linear filters applied to the GVF vector field (rather than to the original image) are discussed in [17]. A curvature diffusion filter [60] is applied with the LSM to sonographic images of breast. An interactive medical image segmentation (sketch snakes) is introduced in [45,61]. Some preprocessing operations such as the edge detection can be also controlled interactively by a human operator. A preprocessing for density-based segmentation [62] employs histogram adjustment, noise reduction using an iterative dilation [63] and a median filtering to suppress the spike-like noise.

Multi-scale approach combined with the active contours shows much promise as applied general segmentation [64,65] as well as to segmentation of the boundary of the endocardial contour in ultrasound images [46]. The idea is that a rough initial contour can be extracted at the highest level of the multiresolution structure. This crude contour is then used for the initialization of the optimization process at the coarsest level. The multiresolution techniques can be combined with a variety of other preprocessing methods such as the phase portrait analysis [66] which applies directly to the vector field.

GGVF endowed with an appropriate sequence of noise elimination steps remains one of the most popular choices for segmentation of the US images. The method removes gradients produced by the speckles and the tissue-related edges and allows to hand-tune coefficients and the force terms in the corresponding Euler equations. Furthermore, the parameters of the snake can be adjusted depending on the anticipated shape and size of the tumor. However, when the noise related gradients are comparable with the boundary gradients, the diffusion smoothes the false and the true contour points equally. The smoothing after a large number of time steps (iterations) may change the direction of vectors pointing (correctly) towards each other at the true boundary. Besides, GGVF does not include other features such as the directions of the corresponding vector field. Consequently, a weak boundary which generates antiparallel vectors having a small magnitude might be entirely destroyed by the diffusion.

There are several recent variations of the GGVF resistant to noise and characterized by a large capture range and improved accuracy. In particular, Poisson gradient vector field (PGVF) [71,72] is calculated by solving numerically the Poisson equation where the right hand side is obtained from a binary map produced by Canny edge detector. The PGVF is then computed as the gradient of the Poisson solution. The method combined with the genetic algorithm (GA) connecting broken boundaries was applied to automate segmentation of tumors of liver in positron emission tomography [72] and to automatic extraction of face contours [73].

IN_{Est}-GVF (impulse noise estimator) is an attractive modification of GVF which combines anisotropic diffusion with an adaptive median filtering [74]. The model performs well on digital images corrupted by a mixed noise. However, an appropriate size of the filtering window is still an open problem.

The majority of modifications of GVF are still based on the magnitude of the resulting gradient field and do not include the orientation of the vectors. An attempt to include the direction of the gradient vector field is the convolution vector flow [75] (CVF) calculated by convolving the edge map with a user-defined kernel. Since the edges contribute more to the CVF than homogeneous regions, it is beneficial to use kernels similar to the attracting stars or nodes [66]. These configurations are amplified whereas the noise is suppressed. The CVF snakes are characterized by large capture ranges, and converge efficiently to boundary concavities. Additionally, they are more robust to noise and initialization than the standard GVF snakes. However, a possible drawback of CVF is that the weak edges might be overwhelmed by the strong edges along with the noise. This problem is solved by mixing CVF with the standard gradient field using a threshold that determines the edges to preserve. The threshold works similar to the smoothing parameter in GGVF. Furthermore, although this method takes into account the direction of the gradient vector field, it treats the object boundary and the strong noise equally. In other words, gradients invoked by a strong noise (comparable with the boundary) will be amplified as well.

The dynamic directional gradient vector flow (DDGVF) [77] makes use of the gradients in both the x and the y-directions to generate an external force field for the two directions separately. Furthermore, the proposed DDGVF is applied dynamically according to the orientation of snake in each iteration. A directional score is generated. Thus, only the edges with a desired gradient direction participate in the snake deformation [14,76]. However, these methods require that the user locates a point inside the desired object to differentiate the "positive" and "negative" boundaries. Therefore, it is not suitable for fully automatic detection. Besides, our experiments show DDGVF performs poorly on the US images.

This paper introduces a new modification of GGVF to evaluate the local configurations of the vector field and assign each point a direction score. If the configuration includes nearly anti parallel vectors, the corresponding diffusion coefficient gets decreased and the "stopping term" is increased. To the best of our knowledge this modification is the first model which evaluates the relative positions of the vectors (configurations of the GVF) and introduces a continuous directional score of the vector field.

Our second feature is the magnitude of the gray level of the edge map. The novelty of the model is a score evaluated by using clusters corresponding to the background, the shadows/noise and the boundary. The centers of the clusters are used to generate an interpolating function which represents the magnitude. The approach generates an adaptable version of GGVF with a diffusion coefficient evaluated automatically for each individual US image. We show that the adaptation is as efficient as the standard GGVF with the parameters selected by the "brutal force" ("trial and error") approach *individually for every image*.

The algorithm has been tested on a set of ground truth images hand-drawn by leading radiologists with the Queen Sirikit Center for Breast Cancer of Bangkok [86]: Vongsaisuwon, Chulakadabba and Manasnayakorn.

The error was evaluated in terms of the maximum and the average Hausdorff distance (contour based measure) as well as in terms of the percentage of the true positives (pixel based measure). The tests show that the proposed techniques lead to a better convergence and better segmentation accuracy with the reference to the conventional GGVF snakes. Finally, we tested our approach against the above mentioned modifications of GGVF, i.e. Poisson gradient vector flow [71–73], mixed noise vector flow [74] and the convolution vector flow [75]. The numerical results show a significant improvement in terms of the segmentation accuracy.

2. Gradient vector flow snakes

An active contour or snake is a parametric curve $X(s) = (x(s), y(s)), s \in [0, 1]$ evolving inside the image domain so that it eventually attaches itself to the boundary of the object of interest.

The evolution of the snake is governed by Euler equations corresponding to an energy functional defined by

$$E = \frac{1}{2}\int_0^1 \left(a\left|\frac{dX}{ds}\right|^2 + b\left|\frac{d^2X}{ds^2}\right|^2 \right) + E_{ext}(X)ds, \tag{1}$$

where the weighting parameters a and b control the snake's tension and rigidity.

The minimum of the functional is supposed to be a curve which approximates a boundary of the object of interest. Although this claim has never been proven theoretically for realistic assumptions such as the presence of noise, false objects, speckles, low contrast areas etc, a strong rationale behind it is variational functional (1).

The corresponding Euler equation is given by

$$a\frac{d^2X}{ds^2} + b\frac{d^4X}{ds^4} + \nabla E_{ext} = 0. \tag{2}$$

The first (tension) term establishes an equidistribution of points along the resulting curve whereas the second (stiffness) term

ensures against large curvatures. Finally, E_{ext} is the external energy which pulls the snake towards the desired object boundaries.

A very popular extension of the gradient field is the gradient vector flow (GVF) originally proposed by Xu and Prince [36,37]. The technique replaces a "raw" gradient vector field derived from the image edges by a vector field which minimizes a certain functional which extends the large gradients far from the boundary and smoothes the gradients caused by noise. The GVF is a solution of a linear elliptic equation given by

$$\mu\nabla^2 V - (V - \nabla f)|\nabla f|^2 = 0, \tag{3}$$

where ∇f is the gradient field derived from the edge map of the image. For instance, $f = |\nabla I|$, where I is the gray level of the edge map. A variety of edge detectors such as the Canny or Sobel detectors can be applied to evaluate $|\nabla I|$.

Eq. (3) is the Euler equation for the following functional

$$\mu \iint \left(u_x^2 + u_y^2 + v_x^2 + v_y^2\right) dxdy + \iint |\nabla f|^2 (V - \nabla f)^2 dxdy. \tag{4}$$

The first integral produces a smoothly varying vector field $V = (u(x, y), v(x,y))$, while the second integral encourages the vector field to approach ∇f where $|\nabla f|$ is large. Furthermore, Eq. (3) is solved by treating V as a function of a pseudo-time and by performing numerical iterations as follows:

$$V^{n+1} = V^n + \tau'\left(\mu\nabla^2 V - (V - \nabla f)|\nabla f|^2\right)^n, \tag{5}$$

where n is the iteration number and τ' is the iteration parameter (the pseudo time step). Note that, iterations (5) can be interpreted as solving numerically a heat equation given by

$$\frac{\partial V}{\partial t} = \mu\nabla^2 V - (V - \nabla f)|\nabla f|^2. \tag{6}$$

However, the uniform diffusion μ often produces excessive smoothing. Therefore, Xu and Prince [38] extended the GVF technique by introducing spatially varying coefficients to decrease the smoothing effect, namely,

$$\frac{\partial V}{\partial t} - g(|\nabla f|)\nabla^2 V - h(|\nabla f|)(\nabla f - V) = 0. \tag{7}$$

The improved version of the GVF is called the generalized gradient vector flow (GGVF). The weighting functions g and h depend on the gradient of the edge map so that in the proximity of large gradients g gets smaller whereas h becomes larger. In [14] the following diffusion and "attraction" functions have been proposed

$$g(|\nabla f|) = e^{-(|\nabla f|/K)}, \quad h(|\nabla f|) = 1 - g(|\nabla f|), \tag{8}$$

where K is a calibration parameter.

Introduce a multi-feature diffusion g as follows:

$$g(s_1, s_2, \ldots, s_n) = e^{-\prod_{i=0}^{n} F_i(s_i)}, \tag{9}$$

where s is the normalized feature vector: $0 \leqslant s_i \leqslant 1$ and F_i are non-negative monotone increasing score functions such that $F_i(0) \geqslant 0$ and $F_i(1) \geqslant F_i(0)$, where $F_i(1)$, $F_i(0)$ show the relative importance of the feature i. Note that if $F_i(0) = 0$, F_i works like logical "and", so that if s_i is close to zero $\prod_{i=0}^{n} F_i$ is also close to zero which in turn invokes large diffusion. Therefore, if $F_i(0) = 0$, the feature s_i must be present at the boundary so that $\prod_{i=0}^{n} F_i \neq 0$.

On the other hand if $F_i(0) > 0$, it means that the feature may not be present at the boundary given that other features are prominent.

We consider two features: the local direction of the vector field s_D and the magnitude of the gradient s_M. In other words

$$g(s_M, s_D) = e^{-F_M(s_M)F_D(s_D)}, \tag{10}$$

where s_M, s_D is the magnitude and the direction score of the vector field respectively and F_M, F_D are the corresponding score functions.

Note that F_M, F_D must be monotone decreasing functions. Moreover, defining the score functions at $s = 0$ is important. For instance if $F_M(0) = 0$ than this point is not considered as the boundary point irrespectively of the second feature. On the other hand, if $F_M(0) = a > 0$ then if the second feature is strong, the combination of features (10) can still detect the boundary.

3. Preprocessing with the hierarchical fuzzy C-mean clustering

Preprocessing is a crucial part of the snake-based segmentation. It is well known that without an appropriate filtering and further preprocessing, the snake based segmentation is usually unsuccessful. First, we apply the classical Lee [54], Frost [55] or Kuan [56] filters which work equally good for our particular application. The filters are based on the balance between straightforward averaging in homogeneous regions and the leaving the image intact where edges and point features exist. This balance depends on the coefficient of variation inside the moving window. Noise reduction is followed by quadratic contrast enhancement [68].

Next, we partition the image using the hierarchical C-mean clustering algorithm based on the dendogram. The algorithm is similar to hierarchical clustering [69]. First, the top down approach is applied in such a way that the clusters with large ratio of the between-class/within-class variance called the F-ratio were kept undivided whereas other clusters are allowed to be split. The resulting configuration is fed to the bottom up procedure which define the final set of clusters. In this case the clusters with high F–ratio are not allowed to be merged. Our numerical experiments show that this modification of the standard clustering approach works very well on the US images.

As an introductory example consider the accuracy evaluation of the GGVF applied to a sample US tumor shown in Fig. 1. The edge maps obtained by the Canny edge detector with and without the proposed clustering are shown in Fig. 1(b) and (c) respectively. Clearly, the quality of edge map (b) is inappropriate whereas the edge map (c) is acceptable. The results of accuracy evaluation in Table 1 are given in terms of a Hausdorff distance (H_1 and H_2 respectively, see definitions of the Hausdorff distance in Section 6). The parameters of the standard GGVF were hand tuned to achieve possible accuracy.

Table 1 shows that the accuracy of a segmentation applied to the preprocessed image exceeds the accuracy obtained with the raw image by 50% (47 and 96%). The number of snake iterations after the preprocessing decreased considerably as well.

We tested the proposed preprocessing against other popular methods such as the region growing, morphological operations and the adaptive Otsu threshold. For the majority of the US images, the hierarchical clustering can be adjusted in such a way that it works slightly or even considerably better.

4. The magnitude score

Recall that the diffusion coefficient (10) is given by

$$g(s_M, s_D) = e^{-F_M(s_M)F_D(s_D)},$$

where s_M, s_D is the magnitude and direction score of the vector field respectively and F_M, F_D are the corresponding score functions. The conventional diffusion coefficient used by GGVF is given by $g(s_M) = e^{-\frac{s_M}{K}}$, where K is a single tuning parameter. Our model employs a rational function $F_M(s_M) = -\frac{s_M}{K(s_M)}$, where $K(s_M)$ is a monotone Hermite cubic spline such that $K(s_M) > 0$, $K'(s_M) < 0$, $\forall s_M$. We will call this approach the dynamic – K since the coefficient is

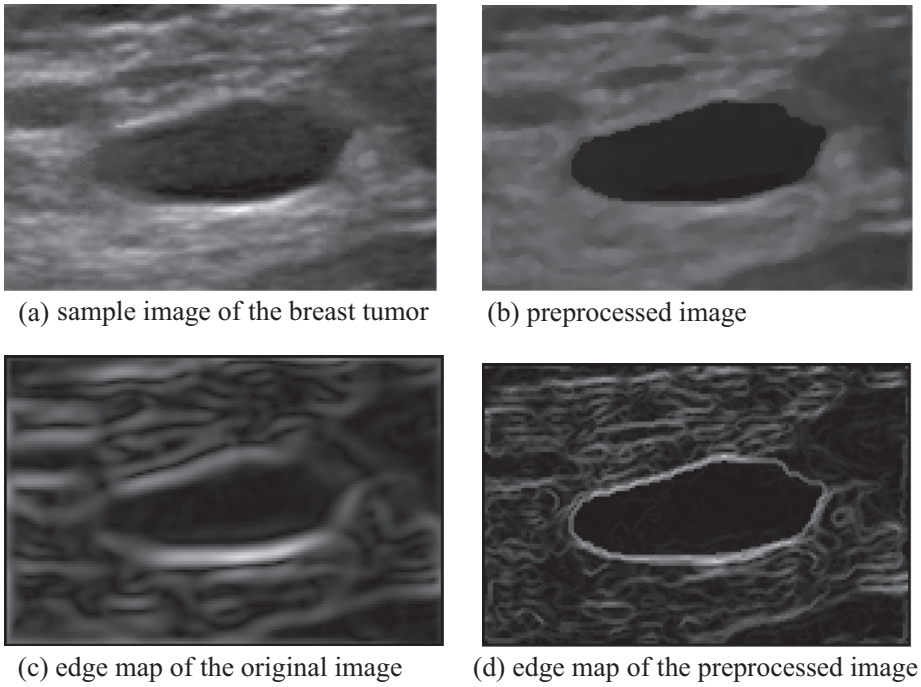

(a) sample image of the breast tumor (b) preprocessed image

(c) edge map of the original image (d) edge map of the preprocessed image

Fig. 1. Hierarchical fuzzy C-mean preprocessing.

Table 1
Accuracy of the COFFA-GGVF snake with and without proposed preprocessing.

Method/criterion	Without, preprocessing the best $K = 0.06$	Preprocessing		
		GGVF, $K = 0.11$	Adaptive K + GGVF	The proposed method
TP	62.6310	98.3132	98.3756	98.6841
H_1	6.7569	3.9621	3.6815	3.2559
H_2	2.9162	2.4632	2.3645	2.3336
# of snake iterations	170	135	90	65

automatically evaluated for every image and changes depending on the position of the pixel.

The polynomial is generated using significant clusters of the edge map. The clusters are generated by the standard fuzzy C-mean method. Usually, the algorithm automatically generates four clusters corresponding to background, noise, shadows and the boundary of the tumor. The centroid of each cluster is selected as the representative of the cluster and the corresponding Hermite polynomial is constructed so that $F_M(s_i) = \zeta_i$, where ζ_i are selected manually. However, if the cluster of shadows is not well defined, only three clusters are generated. Finally, $F_M(0) = 0$. Therefore, if gradient of the edge map is equal to zero, the diffusion reaches its maximum $g(s_M, 0) = 1$. The Hermite polynomial is the monotone piecewise cubic Fritsch–Carlson spline [67] constructed by using the slopes of the secant lines between the successive points and adjusting the slopes to ensure monotonicity. After the preprocessing, the evaluation of the interpolated spline is equivalent to that of the standard Hermite spline. An introductory example in Fig. 2 demonstrates the benefits of the proposed approach applied to a synthetic "tumor" in Fig. 2(a). Fig. 2(b)–(d) show the best contour obtained on the vector field after 1000 GGVF-iterations for $K = 0.1$, 0.2 and 0.3. The resulting snake is very sensitive to the K-variations. Even a small deviation from the best choice of the parameter K in Fig. 2(d) (compare $K = 0.1$ and $K = 0.12$) leads to a substantial inaccuracies (Fig. 2(b)–(d)). As opposed to that, the solution obtained by using the dynamic (adaptive) K does not require any trial and error runs (Fig. 2(f)). Moreover, our forthcoming experiments show that GGVF equipped with the dynamic K usually converges to a meaningful solution whereas the exponential diffusion often destroys the boundary of the desired object.

5. The direction score

This section introduces a new modification of the Continuous Orientation Force Field Analysis (COFFA) [49] to generate the direction (orientation) score. Next, we show how the score can be incorporated into GGVF (10). Recall that at the boundary of the object the vector field consists of antiparallel vectors. In this case the diffusion coefficient $g(s_D, s_M)$ must be small and the "stopping coefficient" $h(s_D, s_M)$ must be large. As opposed to that, parallel vectors corresponding to a background should entail large diffusion, so that small noise is smoothed and the large gradients along the boundary propagate through this area. COFFA measures a deviation from an ideal anti-parallel position. The measure is then used to generate a score vector. In order to capture the direction along which the vectors are aligned the most, the algorithm employs a rotating window. For each orientation of the window the vector field is interpolated into the corners of the window (Fig. 3).

Next, $\varphi(\theta_1, \theta_2)$ is the deviation of the vectors at the two opposing corners from the direction corresponding to the orientation of the window. The closer the two vectors are to the prescribed direction the greater is $\varphi(\theta_1, \theta_2)$.

The maximum response $\varphi(\theta_1, \theta_2)$ shows how close to the anti-parallel position the vector field is in the locality of the candidate boundary point. In order to construct the membership function

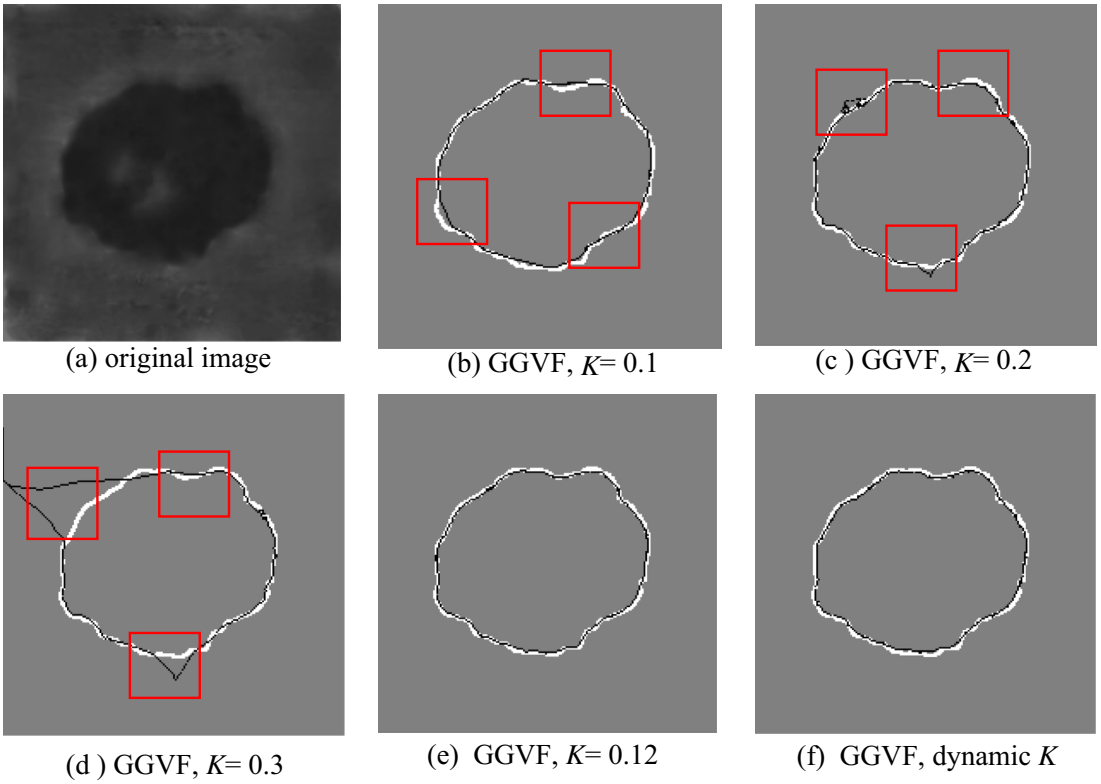

Fig. 2. Adaptive (dynamic) K vs. the exponential diffusion.

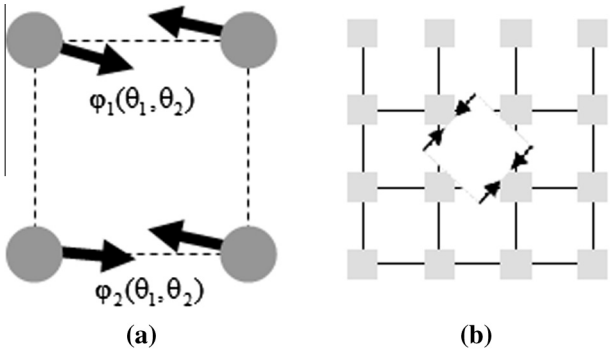

Fig. 3. (a) The direction score as the vector alignment measure (b) the rotating window.

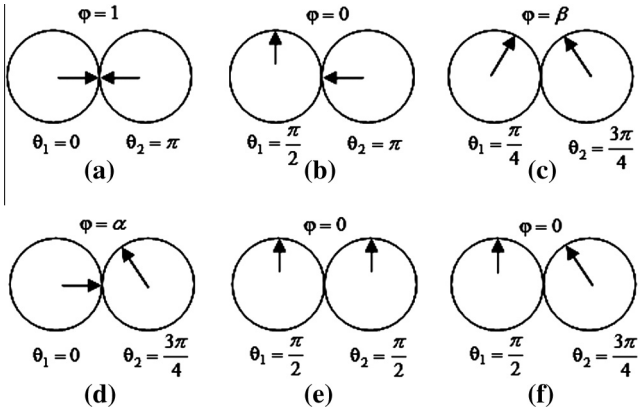

Fig. 4. (a)–(f) The standard positions.

$\varphi(\theta_1,\theta_2)$ we use two dimensional interpolation techniques with a few control points. The measure $\varphi(\theta_1,\theta_2)$:$([0,2\pi]\times[0,2\pi])\to[0,1]$ is constructed on a triangle $\{(0,\frac{\pi}{2}),(\frac{\pi}{2},\frac{\pi}{2}),(\frac{\pi}{2},\pi)\}$ using interpolating points at the corners and in the middle of each side of the triangle. The following conditions at the interpolating points are used:

$$\varphi(0,\pi)=1,\quad \varphi\left(\frac{\pi}{2},\pi\right)=0,\quad \varphi\left(\frac{\pi}{4},\frac{3\pi}{4}\right)=\beta,$$
$$\varphi\left(0,\frac{3\pi}{4}\right)=\alpha,\quad \varphi\left(\frac{\pi}{2},\frac{\pi}{2}\right)=0,\quad \varphi\left(\frac{\pi}{2},\frac{3\pi}{4}\right)=0,$$

where α and β are the design values (see Fig. 4(a)–(f) respectively).

Suppose that $\varphi(0,\frac{3\pi}{4})=\alpha=0.5$ (Fig. 4(d)). It means that the measure of position (d), deviating from the ideal position by $\frac{\pi}{4}$, is 50% of the what we assign in the ideal case when the deviation is zero.

Furthermore, the six positions define a quadratic polynomial given by

$$\varphi(\theta_1,\theta_2)=a_1\theta_1^2+a_2\theta_1\theta_2+a_3\theta_2^2+a_4\theta_1+a_5\theta_2+a_6. \tag{11}$$

Once coefficients a_i are evaluated, $\varphi(\theta_1,\theta_2)$ is extended to $[0,2\pi]\times[0,2\pi]$ symmetrically, thus, becoming a piecewise quadratic function.

Note, that if $\alpha=\beta=\frac{1}{2}$, then (11) becomes a bilinear function given by $(1-\frac{2}{\pi}\theta_1)(1-\frac{2}{\pi}\theta_2)$. Furthermore, $\varphi(\theta_1,\theta_2)$ applies to rotating window W_γ (Fig. 2) to produce a sequence of two dimensional score vectors $s_\gamma=(\varphi_1,\varphi_2)_\gamma$, where γ is the rotation angle.

The vectors are normalized as follows $s_{\gamma,\text{new}}=\frac{s_\gamma}{\max|s_\gamma|}$. Finally, the directional score $s_D=\min_\gamma|s_{\gamma,\text{new}}|$. We assume that the true contour points form large clusters characterized by $s_D>1-\delta$, where δ is an appropriate threshold. Besides the true boundary

points must belong to relatively large continuous segments, whereas the false contour points belong to short segments. Consequently, appropriate edge detection methods such as [42–44] can be applied.

COFFA can be applied in the iterative way as follows. First, the GGVF is applied to the raw gradient field of the edge map ∇f to obtain the vector function $V(x,y) = (u(x,y), v(x,y))$. Next, we measure the COFFA score $s_D(x,y)$ and run an iterative improvement of s_D by obtaining a new the vector function $V(x,y)$. However, using the iterative COFFA-images slows down the algorithm. Besides, this procedure may lead to numerical instabilities. This version of the algorithm calculates s_D only once and uses the corresponding directional score in the subsequent calculations. The score-function $F_M(s_M)$ is non-linear and is based on an adaptive polynomial interpolation. An introductory example in Fig. 5 illustrates the benefits of the proposed approach. The standard GGVF snake applied to the image depicted in Fig. 5(a) with $K = 0.3$ generates an incorrect boundary in Fig. 5(b). However, COFFA-GGVF applied with the same K converges to correct geometries of the object in Fig. 5(c).

6. Numerical experiments

This section presents numerical experiments tested on a ground truth contours obtained from a series of breast tumor US images. The ground truth was hand-drawn by leading radiologists with Queen Sirikit Center for Breast Cancer of Bangkok [85]. The accuracy is defined as a percentage of true positive (TP) points with the reference to the true boundary. A contour point is considered to be a true positive point if a point in the ground truth image belongs to the true contour. The accuracy is also evaluated in terms of the Hausdorff distance (H_1) given by

$$\mathrm{dist}_{H_1}(X,Y) = \max\{\max_{a\in X}\min_{b\in Y}||a-b||, \max_{b\in Y}\min_{a\in X}||a-b||\}, \tag{12}$$

where $\|\ \|$ denotes the Euclidian distance, X the ground truth contour and Y the resulting contour. The averaged Hausdorff distance (H_2) is obtained from (12) by replacing the internal maximum by averaging. In order to obtain a dimensionless estimate (H_3) the Hausdorff distance (12) is divided by the length of the true contour L_Y as follows

$$\mathrm{dist}_{H_3}(X,Y) = \frac{\mathrm{dist}_{H_1}(X,Y)}{L_Y}\xi, \tag{13}$$

where the normalizing coefficient $\xi = 1000.0$.

Note that H_2 is not a distance in a rigorous mathematical sense, because it does not satisfy the triangle inequality. However, experiments [78] show that H_2 is the best for matching objects based on their edge points.

Finally, we evaluate the robustness of the method by its numerical convergence. Let T_n be the number of true positives and let Y_n be the snake contour at iteration n. If for some n and k_0

$$|T_{n+k} - T_n| < \varepsilon_T \quad \text{and} \quad |\mathrm{dist}_{H_1}(Y_{n+k}, Y_n) - \mathrm{dist}_{H_1}(Y_{n+1}, Y_n)| < \varepsilon_H, \quad \forall k \leqslant k_0 \tag{14}$$

we will say that the method converges. Here, k_0 is the number of iterations during which the accuracy estimates are stable and ε_T, ε_H the required tolerance [51].

Denote the proposed method by COFFA-GGVF-DYK, where DYK stands for the dynamic choice of K combined with Hermite interpolation proposed in Section 3.

We test the proposed method against the classical GGVF as well as against recent modifications of GGVF, namely, the Poisson gradient vector flow (PGVF), $\mathrm{IN}_{\mathrm{Est}}$-GVF vector flow, convolution vector flow (CVF) and dynamic directional gradient vector flow (DDGVF) explained in Introduction.

Example 1 (*Low contrast malignant tumor*). Fig. 6(a) displays the original US image. Fig. 6(b) shows the image after contrast enhancement. Furthermore, we show only contrast enhanced images, although in order to prove the efficiency and robustness our method was run on the original low contrast images. The ground truth images such as in Fig. 6(b) were outlined leading radiologists with the Queen Sirikit Center for Breast Cancer of King Chulalongkorn Memorial Hospital, Bangkok Thailand.

The results obtained with GGVF and several versions of the proposed COFFA-GGVF are shown in Fig. 6(c) and (d). The numerical evaluation of the accuracy of the extractions is given in Table 2. The accuracy is estimated in terms of true positives (TP) and the Hausdorff distance H_1, H_2 and H_3 introduced above.

Table 2 indicates convergence of the methods and the best accuracy throughout 5000 iterations. Since the conventional GGVF often does not converge, the best accuracy was recorded at some transitional iteration step. However, a criterion to terminate the GGVF iterations if they do not converge in the classical sense is an open problem. Therefore, the GGVF accuracy is actually overestimated. Clearly, our proposed method outperforms GGVF. First of all, it always converges. Second, COFFA-GGVF-DYK with the adaptive K outperforms GGVF with the best K found by the trial end error method. The adaptive method does not require training and adapts K automatically. The adaptive K employs a monotone Hermite spline interpolation displayed in Fig. 7.

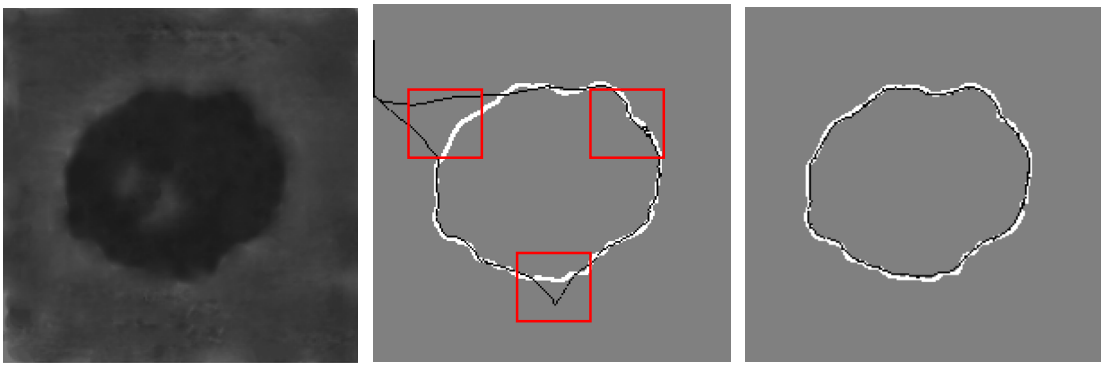

(a) original image (b) GGVF, $K = 0.3$ (d) COFFA-GGVF , $K = 0.3$

Fig. 5. COFFA vs. the exponential diffusion.

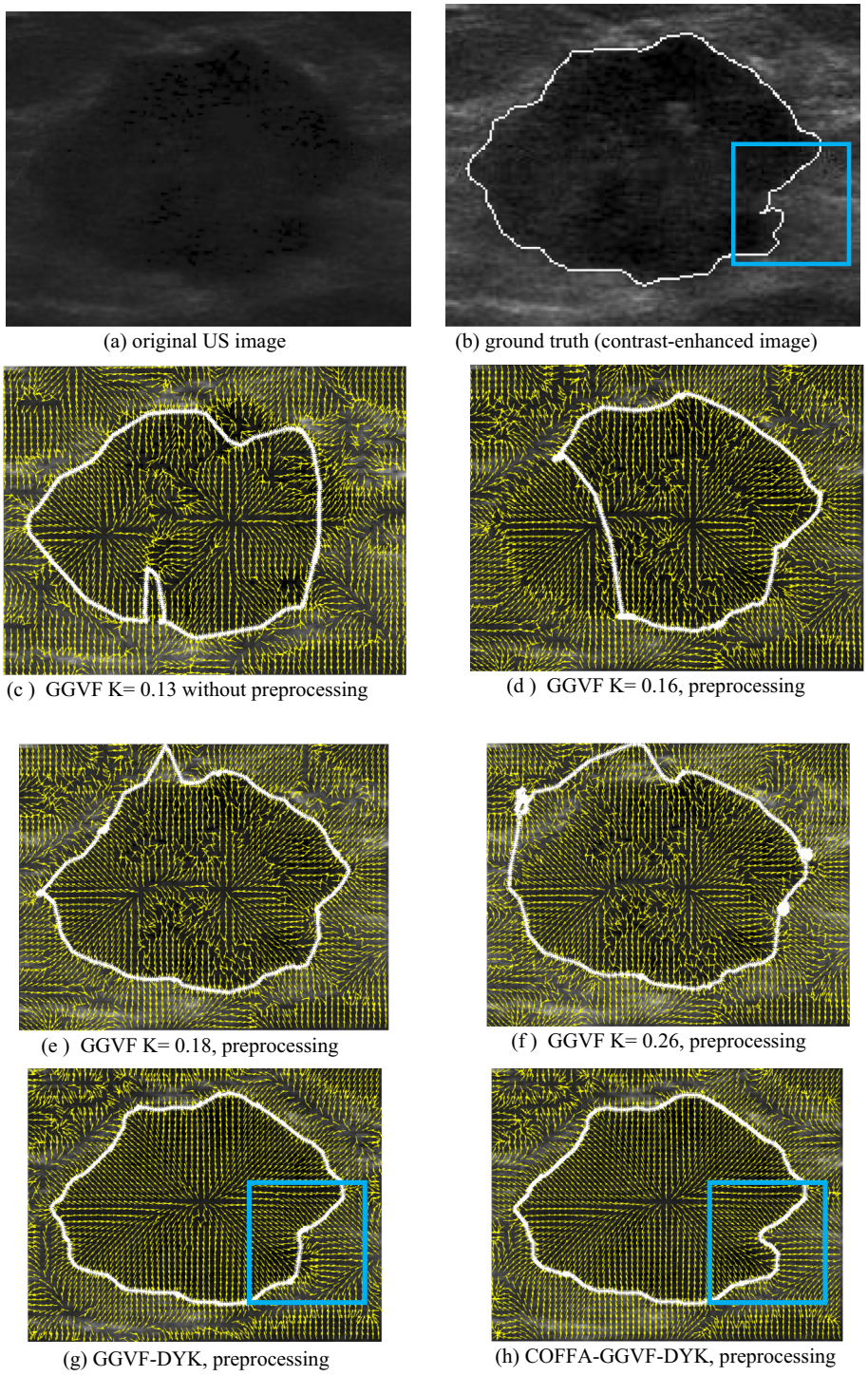

(a) original US image (b) ground truth (contrast-enhanced image)

(c) GGVF K= 0.13 without preprocessing (d) GGVF K= 0.16, preprocessing

(e) GGVF K= 0.18, preprocessing (f) GGVF K= 0.26, preprocessing

(g) GGVF-DYK, preprocessing (h) COFFA-GGVF-DYK, preprocessing

Fig. 6. Extraction results by the proposed method vs. standard GGVF.

The classical explicit numerical scheme was employed which converges if $4g_{\max}\tau < 1$ [37]. This condition was satisfied for every experiment. However, GGVF iterations may diverge when $g(|\nabla f|)$ is too small, that is, the parabolic Eq. (7) degenerates. This case requires special numerical procedures for parabolic equations with singularities [70]. For instance, if $g(|\nabla f|) \equiv 0$, (7) is no longer parabolic. Therefore, boundary conditions (required for uniqueness of the solution) cannot be satisfied.

However, the proposed polynomial interpolation does not change as fast as the exponential diffusion. Besides we freeze the numerical solution when $g(|\nabla f|)$ is close to zero. These procedures help to maintain the numerical stability and provide the convergence even when the simple explicit scheme is employed.

Finally, in many cases the accuracy of GGVF is very sensitive to variations of K. Consider a graph of TP vs. K in Fig. 7. The maximum accuracy $\mathrm{TP}_{\max} = 89\%$ is achieved at $K = 0.185$. Let us define an acceptable range as $\{K : \mathrm{TP} \leqslant 0.99\mathrm{TP}_{\max}\}$. Then $K \in [0.17, 0.225]$ with the average accuracy of 88% within this interval. It is a relatively large interval, however, the accuracy drops abruptly when $K < 0.17$ (Fig. 8). For instance, for $K = 0.16$ the accuracy is only 83%. The adaptive procedure adopted by COFFA-DYK increases the variability of the permissible diffusion $g(s)$, thus, resulting in

Table 2
Example 1. Accuracy and convergence of GGVF and COFFA-GGVF-DYK.

Criterion/method	No preprocessing GGVF + best $K = 0.13$	Preprocessing			
		GGVF, K varies		GGVF-DYK	COFFA-GGVF-DYK
		Best $K = 0.18$	Acceptable range: 0.17–0.22		
TP	39.1975	89.1901	88.0814	91.3580	93.0329
H_1	23.2402	8.1519	8.9413	6.1855	5.1173
H_2	9.1462	1.0329	1.0724	0.9059	0.7638
H_3	20.6927	1.9475	2.0220	1.8642	1.5716
Snake convergence	Yes	Yes	Yes	Yes	Yes
GGVF convergence explicit scheme	No	No	No	Yes	Yes

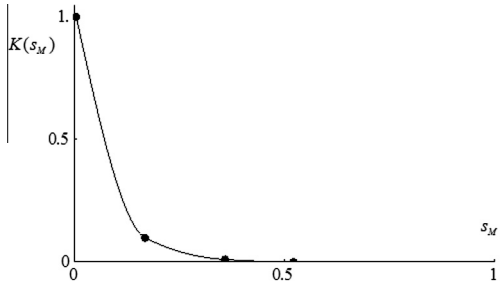

Fig. 7. Adaptive K: the Hermite polynomial passes through the center of the intensity clusters (black dots) corresponding to the background, noise, "shadows" and the boundary.

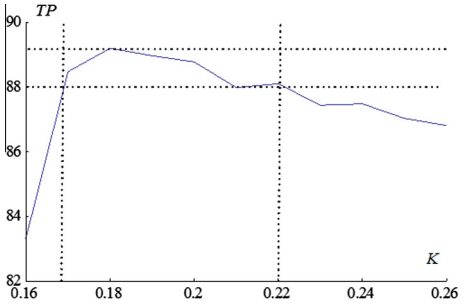

Fig. 8. Accuracy of GGVF vs. the diffusion coefficient K.

the same or even better segmentations with the reference to the best GGVF performance.

According to Table 2 the best accuracy has been achieved by the proposed method with the maximum Hausdorff error $H_1 = 5.0$ pixels and the average Hausdorff error $H_2 \approx 1$. It means that on average, the actual contour deviates from the true contour by only 1 pixel. Finally, $H_3 = \frac{H_1}{L_X}\xi$, where $\xi = 1000.0$. Therefore, $H_3 = 1.4$ achieved by COFFA-GGVF-DYK, indicates that the maximum amplitude of the deviation of the resulting contour from the ground true contour is 0.15% of the total length of the true contour. Assuming that the tumor is round, the "radius" of the tumor $R_X = \frac{L_X}{2\pi}$. Therefore, the ratio $\frac{H_1}{R_X} = 2\pi 0.15\% \approx 1\%$.

Consider segmentation results presented in Fig. 6(c)–(h). GGVF—DYK and COFFA-GGVF-DYK generate star-like patterns ideal for using the expanding snakes (Fig. 6(a)) whereas GGVF with the best $K = 0.18$ generates multiple stars (unwanted internal boundaries). Finally, only COFFA-GGVF-DYK is able to resolve the corner on the right side of the image (Fig. 6(b), (g) and (h)). The adaptive diffusion coefficient is give in Fig. 7. The accuracy of GGVF vs. the diffusion coefficient K is shown in Fig. 8. Consider the accuracy (TP) vs. the iteration number in Fig. 9. Clearly the standard GGVF does not converge whereas the proposed method does.

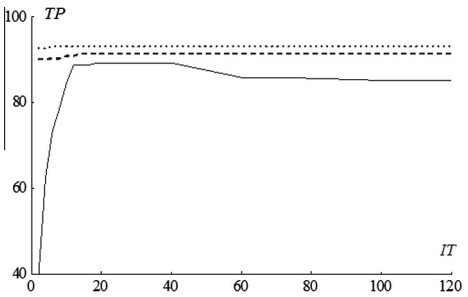

Fig. 9. Convergence of the proposed method vs. the conventional GGVF: solid line – GGVF, dashed line GGVF-DYK, dotted line COFFA-GGVF-DYK.

The accuracy of GGVF in terms of TP reaches its peak at 6th–9th iteration. However, the diffusion destroys the boundary decreasing the number of the true positives.

Example 2 (*A malignant tumor. Complicated shape. High level of noise*). The tumor in Fig. 10(a) is characterized by concavities and spikes which are usually hard to detect using a snake based approach. However the results are similar to Example 1. Table 3 shows that COFFA-GGVF-DYK outperforms the standard GGVF even for a hand-tuned K. Note that optimal K for GGVF for Example 2 is very different from K obtained in Example 1. The optimal $K = 0.18$ for the tumor from Example 1, however the best $K = 0.13$ for Example 2. Moreover, the acceptable range in Example 1 and 2 is [0.17–0.22] and [0.12–0.13] respectively. The high variability of optimal K in Figs. 7 and 11 means that in general it is not possible to establish a single K for the GGVF model even by training the model on a series of images. Nevertheless, the our proposed model is parameter free. The dynamic K is established automatically and varies from region to region.

Example 3 (*Malignant tumor. Irregular non-round shape*). The method has been tested on a tumor having a non circular shape shown in Fig. 12(a) and (b). This example shows an advantage of COFFA with regard to a conventional edge map. The image has been preprocessed by the Hierarchical Fuzzy C-mean Clustering (Fig. 12(c). The Sobel edge detector and the COFFA applied the image in Fig. 12(c) are displayed in Fig. 12(d) and (e) respectively. COFFA image is characterized by a better visualization of the edge at the boundary of the tumor. Since the visual comparison is subjective, our final test is the accuracy of the resulting snake. The worst and the best GGVF segmentation are shown in Fig. 12(f) and (g) whereas COFFA-GGVF-DYK is displayed in Fig. 12(h).

The accuracy of segmentation is shown in Table 4. COFFA-GGVF-DYK performs similarly to the standard GGVF for the best K selected manually. The acceptable range is quite large $K = 0.06$–0.11 and the accuracy within the acceptable range does

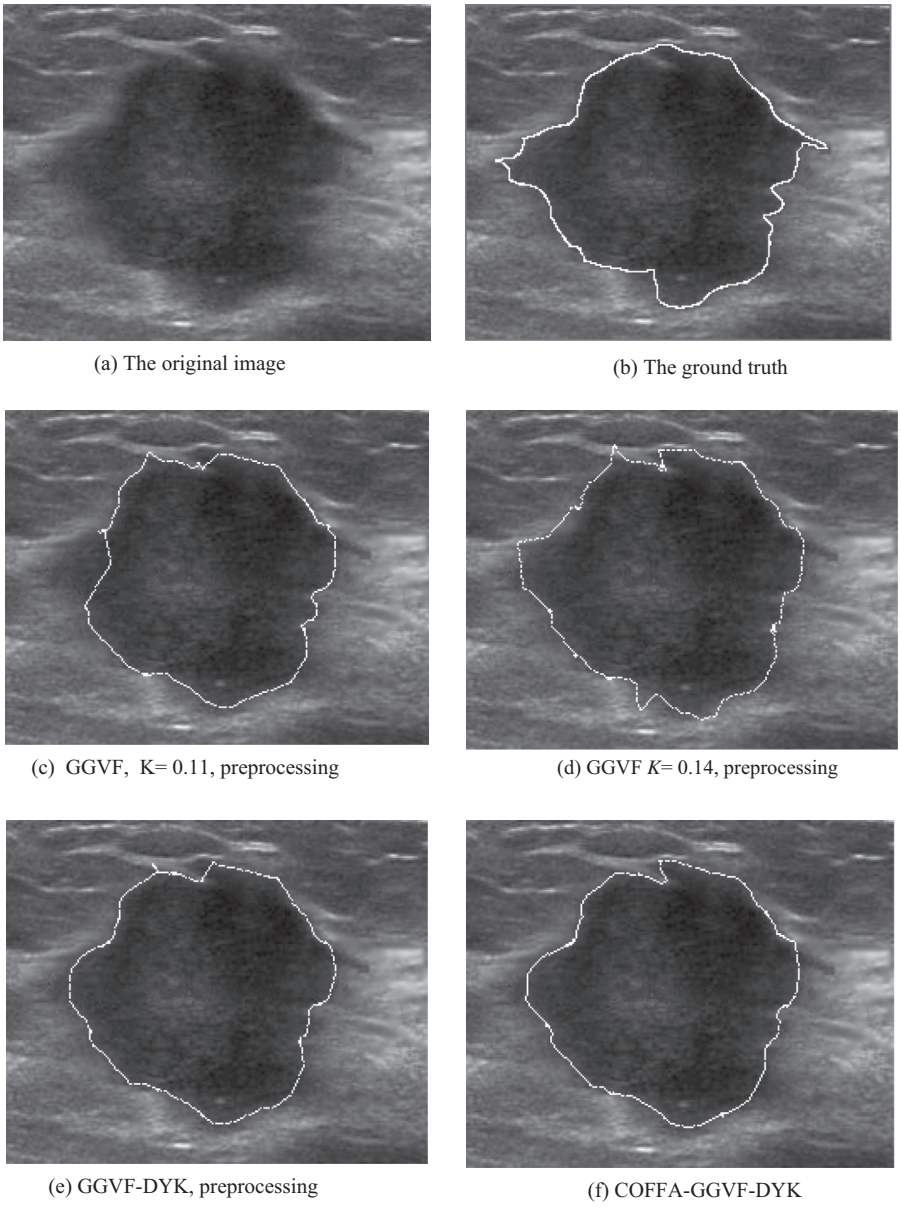

Fig. 10. Extraction results using the proposed method with the reference to the standard GGVF.

Table 3
Example 2. Accuracy and convergence of GGVF and COFFA-GGVF-DYK.

Criterion/method	No preprocessing GGVF + best K 0.09	Preprocessing			
		GGVF K varies		GGVF-DYK	COFFA-GGVF-DYK
		Best K = 0.13	Acceptable range: K = 0.12–0.134		
TP	24.9165	88.0059	88.0050	88.2698	91.0236
H_1	32.0278	7.0881	7.3531	6.6123	5.6857
H_2	23.9605	1.3935	1.3939	1.3660	0.6766
H_3	13.4837	0.7841	0.7843	0.7687	0.3808
Snake convergence	Yes	Yes	Yes	Yes	Yes
GGVF convergence explicit scheme	No	No	No	Yes	Yes

not change considerably. However, it does not overlap with the acceptable range from Example 1 and is very different from the acceptable range in Example 2.

Example 4 (*Sensitivity to initialization*). The proposed method is less sensitive to the position of the initialization Contour and works much better that the conventional GGVF when the initial

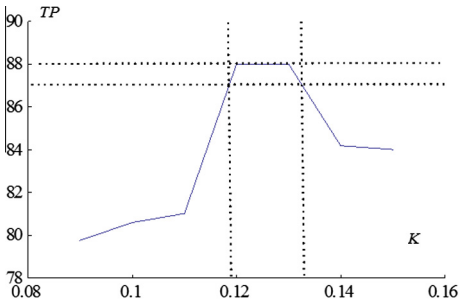

Fig. 11. Accuracy of GGVF vs. the diffusion coefficient K.

snake is far from the boundary. The test tumor and the ground truth are shown in Fig. 13(a) and (b). The snake has been initialized at the distance $d = 5$, 12, 32 pixels from the boundary measured by using Hausdorff distance H_1. The results for each initialization are presented in Table 5.1, Table 5.2 and Table 5.3 respectively and in Fig. 13(c)–(f).

Clearly, when the initial snake is close to the true boundary, the performance of GGVF and COFFA-GGVF-DYK is excellent. For $d = 5$, the accuracy is 99% in terms of true positives and 0.3 in terms of H_2. Moreover, GGVF converges. Yet, increasing the distance leads to a drastic decline in the accuracy of GGVF in all categories: TP, H_1, H_2 and H_3. The noise which was not properly processed by the conventional GGVF attracts the snake leading to huge errors. For $d = 32$ the best performance of GGVF is only 83% in terms of true positives and the maximum deviation from the true contour reaches 29 pixels. However, the proposed method produces a consistent result of 99% true positives and the deviation measured by H_1 is of about 2.14 pixels.

Example 5 (*Testing against recent modifications of GGVF*). In this example we test our techniques against the ground truth segmentations and recent modifications of GGVF, i.e. Poisson gradient vector flow-PGVF [71–73], mixed noise vector flow based on an adaptive noise estimator IN_{Est}-GVF [74] and the convolution vector flow CVF [75]. A short description of each method is presented in Introduction on page 6. The code for generation of the CVF fields was generously provided by the author Li whereas IN_{Est}-GVF and PGVF were replicated following [73,74].

The images include 3 synthetic sets (65 images each) characterized by different levels of noise and 48 real tumor images. The input images are preprocessed by Gaussian smoothing, median filtering and a speckle noise filter. Note that in Examples 1–4 we compare the proposed method with the standard GGVF applied

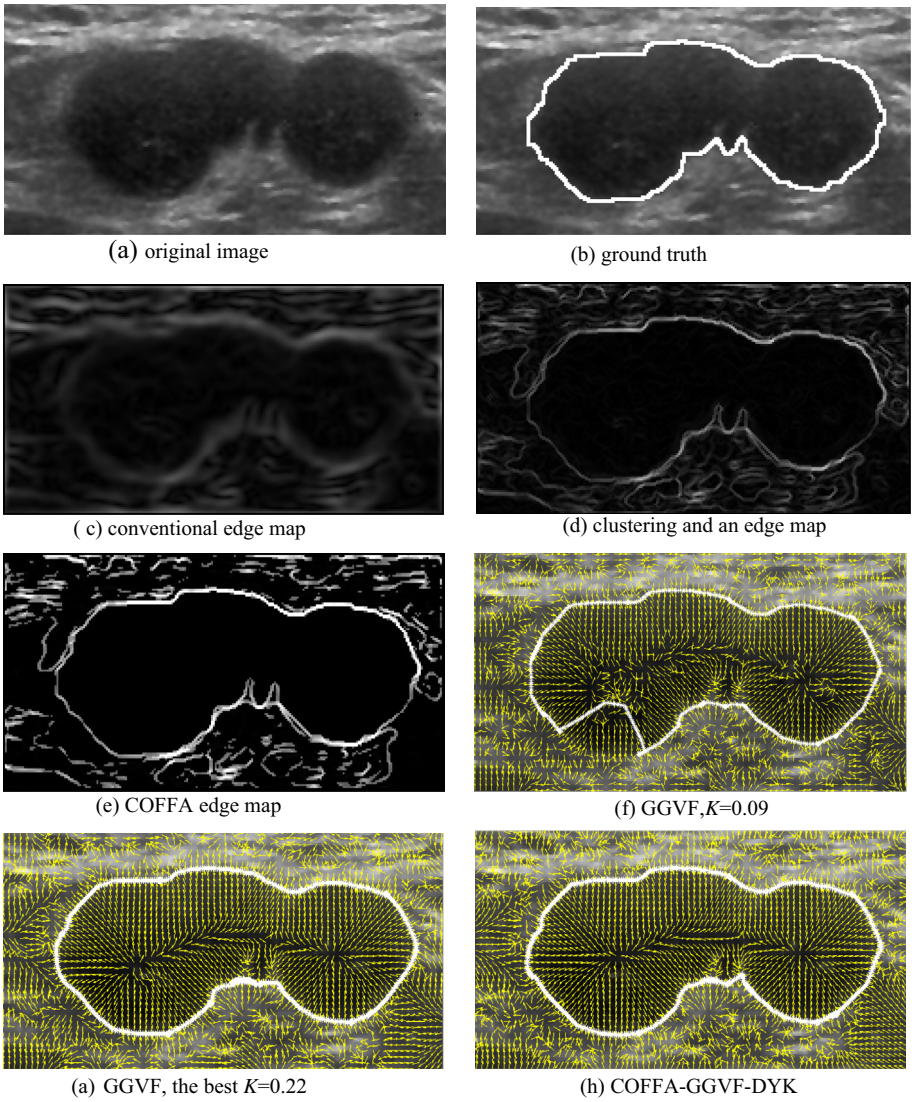

(a) original image

(b) ground truth

(c) conventional edge map

(d) clustering and an edge map

(e) COFFA edge map

(f) GGVF,K=0.09

(a) GGVF, the best K=0.22

(h) COFFA-GGVF-DYK

Fig. 12. GGVF vs. COFFA-GGVF-DYK, Example 3.

Table 4
Example 3. Accuracy and convergence of GGVF and COFFA-GGVF-DYK.

Criterion/method	Non-Preprocessing GGVF + best k 0.11	Preprocessing			
		GGVF K varies		GGVF-DYK	COFFA-GGVF-DYK
		Best K = 0.09	Acceptable range: K = 0.06–0.11		
TP	34.5065	97.7013	97.5448	98.3126	98.4703
H_1	8.3768	5.0984	5.4194	4.8079	4.3071
H_2	1.4893	0.4897	0.5240	0.4495	0.4163
H_3	1.1360	0.3735	0.3997	0.3429	0.3176
Snake convergence	Yes	Yes	Yes	Yes	Yes
GGVF convergence explicit scheme	No	No	No	Yes	Yes

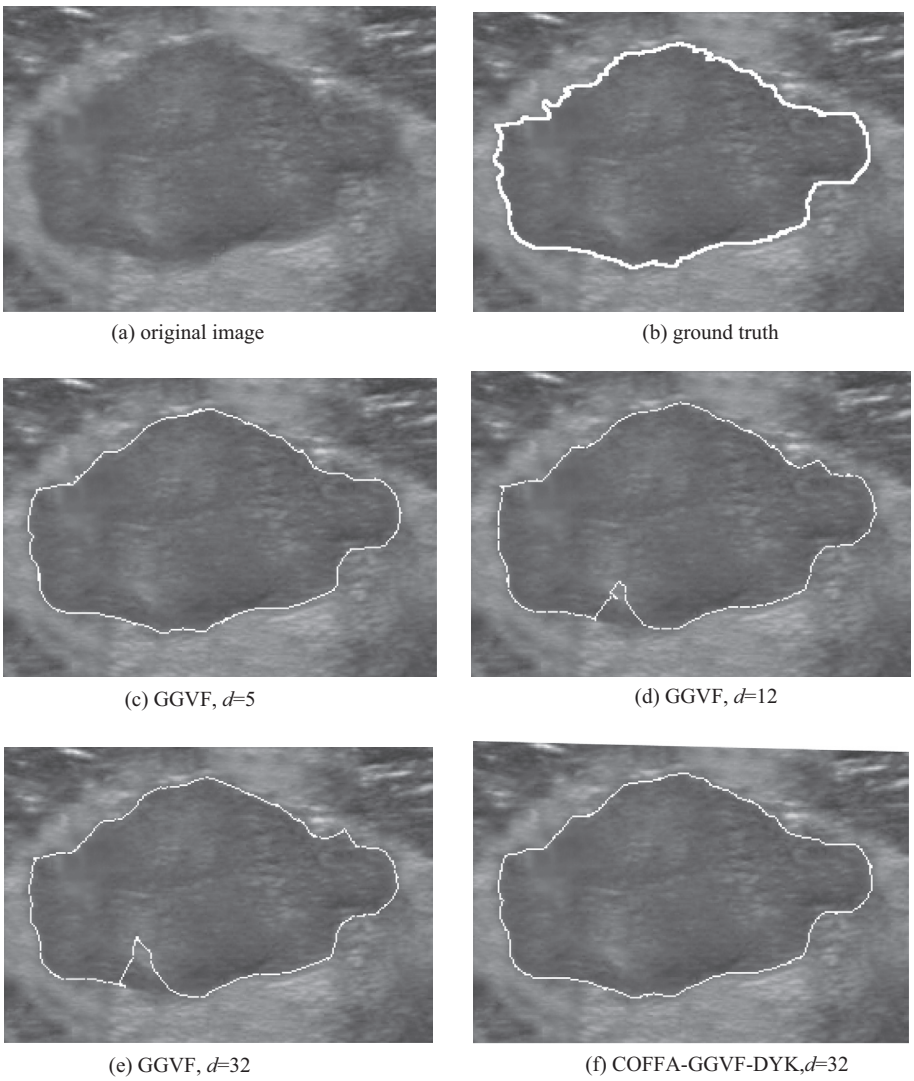

(a) original image (b) ground truth

(c) GGVF, d=5 (d) GGVF, d=12

(e) GGVF, d=32 (f) COFFA-GGVF-DYK,d=32

Fig. 13. GGVF vs. COFFA-GGVF-DYK, Example 4.

Table 5.1
Example 5. Accuracy and convergence of GGVF vs. COFFA-GGVF-DYK, d = 5.

Criterion/method	Preprocessing		
	GGVF, best K = 0.009–0.01	GGVF-DYK	COFFA-GGVF-DYK
TP	99.1028	99.1028	99.1905
H_1	2.1225	2.1472	2.1217
H_2	0.3223	0.3199	0.3088
H_3	0.2027	0.2012	0.1942
Snake convergence	Yes	Yes	Yes
GGVF convergence explicit scheme	Yes	Yes	Yes

Table 5.2
Example 5. Accuracy and convergence of GGVF vs. COFFA-GGVF-DYK, $d = 12$.

Criterion/method	Preprocessing		
	GGVF, best $K = 0.08$	GGVF-DYK	COFFA-GGVF-DYK
TP	88.8755	99.1026	99.1905
H_1	23.1307	2.1680	2.1410
H_2	1.4630	0.3218	0.3104
H_3	0.9201	0.2024	0.1952
Snake convergence	Yes	Yes	Yes
GGVF convergence explicit scheme	No	Yes	Yes

Table 5.3
Example 5.3. Accuracy and convergence of GGVF vs. COFFA-GGVF-DYK, $d = 32$.

Criterion/Method	Preprocessing		
	GGVF, best $K = 0.09$	GGVF-DYK	COFFA-GGVF-DYK
TP	83.7552	99.1025	99.1903
H_1	29.4658	2.1703	2.1461
H_2	3.2775	0.3236	0.3221
H_3	2.0613	0.2034	0.2026
Snake convergence	Yes	Yes	Yes
GGVF convergence explicit scheme	No	Yes	Yes

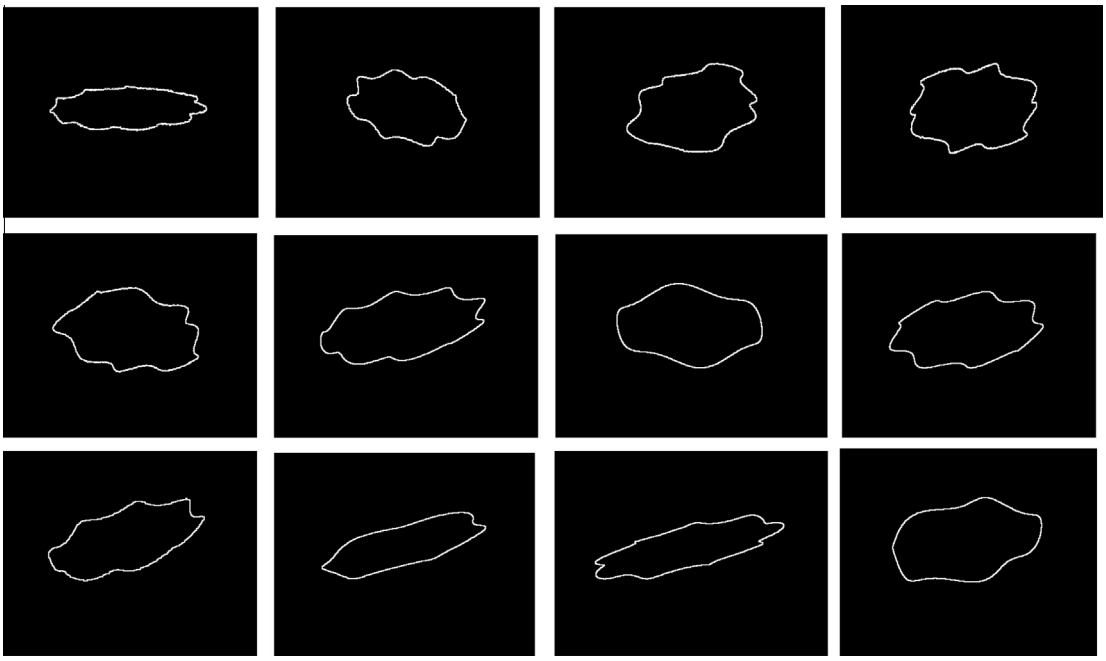

Fig. 14. Examples of synthetic (randomly generated) tumors.

with the best possible set of parameters hand-tuned individually for each image. As opposed to that, Example 5 is a real situation where the parameters of the segmentation methods are evaluated by training.

The 195 (496×401) images of synthetic tumors were generated by using the oval shapes subjected to elastic deformations [85] and trigonometric boundary noise (Fig. 14). 135 images were used for training and 60 for testing. The complexity of the segmentation problem was evaluated by the level of the additive speckle noise (db). The images are characterized by a low contrast measured by $c = \frac{G_{out} - G_{in}}{G_{out}} = 0.27$, where G_{in}, G_{out} the average grey level inside and outside the tumor. Note that the proposed combination of a low contrast and a speckle noise in the range 15–25 db is a challenging problem for segmentation methods. The average distance of the initial snake measured in terms of Hausdorff distance is $H_1 = 28.3$ and $H_2 = 16.0$. The competing methods have been trained with regard to the following parameters:

- IN_{Est}-GVF: the size of the window to suppress the noise, the regularization parameter and the diffusion coefficient of the GGVF,
- PGVG: parameters of the GA (population size and mutation rate) and the diffusion coefficient of the GGVF,
- CVF: the size of the convolution kernel, the design parameter of the kernel, the threshold required to mix the convolution and the gradient vector fields.

Table 6
Accuracy of IN_{Est}-GVF, PGVF and CVF vs. the proposed method. Synthetic tumors.

Noise/criterion/method		IN_{Est}-GVF	PGVF	CVF	COFFA-GGVF-DYK
PSNR = 24 db	% Images, TP > 80%	100%	100%	100%	100%
	Average TP	97.4722	99.83%	99.81%	99.89%
	Average H_1	6.3956	5.1006	5.6978	4.5927
	Average H_2	2.0571	1.6657	2.1047	1.5827
PSNR = 17 db	% Images, TP > 80%	52.63%	78.90%	78.95%	100%
	Average TP	85.71%	88.99%	92.24%	96.17%
	Average H_1	11.9572	9.9474	8.6094	4.7755
	Average H_2	3.4501	2.7706	2.1379	1.6064
PSNR = 15 db	% Images, TP > 80%	NA	NA	52.63%	84.21%
	Average TP			86.23%	91.83%
	Average H_1			14.9318	8.9325
	Average H_2			4.6069	3.3364
# Of training parameters		3	3	3	None

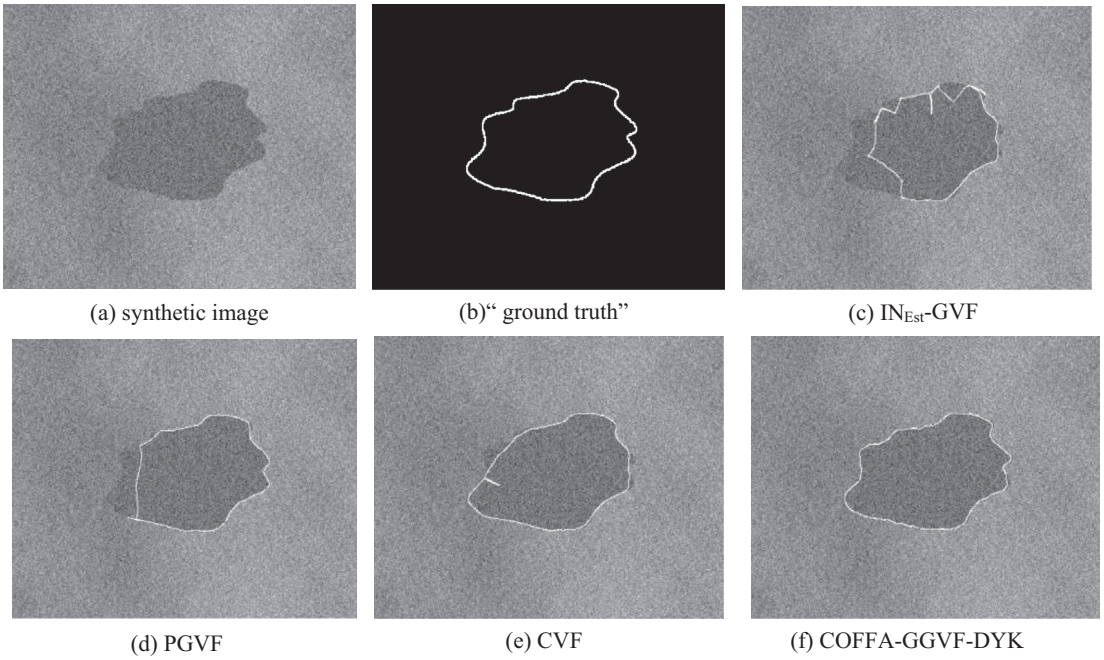

Fig. 15. COFFA-GGVF-DYK vs. selected GVF methods, synthetic images.

COFFA-GGVF-DYK was applied without any training to the same set of 60 testing images. The testing results are presented in Table 6 which displays the percentage of testing images segmented with the accuracy TP > 80%. The actual accuracy is given in terms of TP, H_1 and H_2. For the noise of 24 db IN_{Est}-GVF, PGVF, CVF and COFFA-GGVF-DYK perform equally well in terms of TP, however, the proposed method has a slight advantage in terms of H_1 and H_2. As far as the medium speckle noise of about 17 db is concerned, the COFFA-GGVF-DYK is a definite winner with an overwhelming advantage: 100% of accurate segmentations vs. 79% produced by CVF and PGVF and only 52.5% by IN_{Est}-GVF (Fig. 15). The noise of about 15 db disables the training procedures for IN_{Est}-GVF, PGVF (symbol NA in Table 6). In other words the training fails to produce statistically significant average training parameters. The accuracy of CVF drops down to 53%, however, COFFA-GGVF-DYK segmentation is still successful for 83% of the images with the accuracy of about 91% TP and only 3 pixel average H_2. Finally, PGVF requires a binary image produced by the GA. Therefore, it is sensitive to the Gaussian smoothing. An extensive blurring produced by the Gaussian often breaks down the GA designed to connect the edges. Besides, using the GA, comes at the cost of a factor of 8–10 slowdown in runtime performance compared to COFFA-GGVF-DYK.

Table 7
COFFA-GGVF-DYK vs. IN_{Est}-GVF, PGVF and CVF on real images.

Criterion/method	IN_{Est}-GVF	PGVF	CVF	COFFA-GGVF-DYK
% Images, TP > 80%	64%	64%	71%	79%
Average TP	87.58%	89.86%	89.07%	92.06%
Average H_1	11.5860	8.1425	8.2573	5.1706
Average H_2	2.9513	2.3916	2.4074	1.5099
# Of training parameters	3	3	3	None

Table 7 shows the accuracy of the IN_{Est}-GVF, PGVF, CVF and COFFA-GGVF-DYK applied to 48 images of the real breast tumors. 30 images were used for training and 18 for testing. The proposed method displays a clear advantage in terms of correctly segmented tumors and the accuracy measured by TP, H_1 and H_2 (see also Fig. 16). As before, COFFA-GGVF-DYK was applied without any preliminary training or hand-tuning of the parameters.

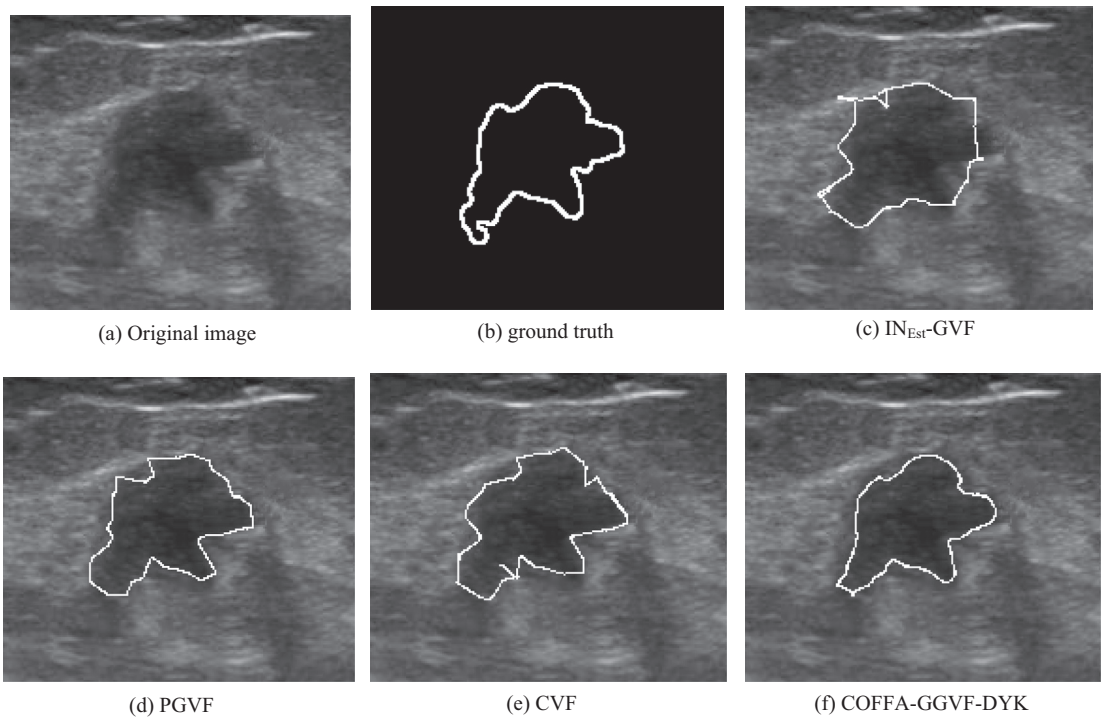

Fig. 16. COFFA-GGVF-DYK vs. selected GVF methods, real images.

7. Conclusions

Based on the adaptive multi feature scheme, the proposed COFFA-GGVF-DYK snake shows much promise as applied to segmentation of the breast tumors. The method generates the same or even better accuracy with the reference to the standard GGVF method equipped with the best set of parameters found individually for a particular image. As opposed to that the proposed method is parameter free and does not require any calibration with regard to the coefficients involved in the smoothing and the stopping term. The numerical experiments show excellent results when applied to the initial contour positioned far from the true boundary. Comparison with recent modifications of GGVF displays considerable improvement in the segmentation accuracy.

Acknowledgments

We acknowledge the codes to compute the convolution vector flows (CVF) generously provided by Dr. B. Li. We wish to thank Dr. Vongsaisuwon, Dr. Chulakadabba and Dr. Manasnayakorn with the Queen Sirikit Center for Breast Cancer of Bangkok for the ground truth images. This research is sponsored by Thailand Research Fund grant BRG5380016 and the Center of Excellency in Biomedical Engineering, Thammasat University of Thailand.

References

[1] M. Kass, A. Witkin, D. Terzopoulos, Snakes: active contour models, International Journal of Computer Vision 1 (4) (1988) 321–331.
[2] F. Lefebvre, G. Berger, P. Laugier, Automatic detection of the boundary of the calcaneus from ultrasound parametric images using an active contour model; clinical assessment, IEEE Transactions on Medical Imaging 17 (1) (1998) 45–52.
[3] Y.S. Akgul, C. Kambhamettu, M. Stone, Extraction and tracking of the tongue surface from ultrasound image sequences, in: International IEEE Computer Society Conference on Computer Vision and Pattern Recognition, Santa Barbara, California, 1998, pp. 298–303.
[4] R. Chung, C.K. Ho, Using 2D active contour models for 3D reconstruction from serial sections, in: Proceedings of the 13th International IEEE Conference on Pattern Recognition, Vienna, Austria, 1996, pp. 849–853.
[5] A. Fenster, S. Tong, H.N. Cardinal, C. Blake, D.B. Downey, Three-dimensional ultrasound imaging system for prostate cancer diagnosis and treatment, IEEE Transactions on Instrumentation and Measurement 47 (6) (1998) 1439–1447.
[6] M.G. Strintzis, I. Kokkinidis, Maximum likelihood motion estimation in ultrasound image sequences, IEEE Signal Processing Letters 4 (6) (1997) 156–157.
[7] D.R. Chen, R.F. Chang, W.J. Wu, W.K. Moon, W.L. Wu, 3-D breast ultrasound segmentation using active contour model, Ultrasound in Medicine and Biology 29 (7) (2003) 1017–1026.
[8] R.F. Chang, W.J. Wu, W.K. Moon, W. Lee, D.R. Chen, Segmentation of breast tumor in three-dimensional ultrasound images using three-dimensional discrete active contour model, Ultrasound in Medicine and Biology 29 (11) (2003) 1571–1581.
[9] M. Cvancarova, F. Albresgtsen, K. Brabrand, E. Samset, Segmentation of ultrasound images of liver tumors applying snake algorithms and GVF, Congress Series 1281 (2005) 218–223.
[10] M. Aleman-Flores, P. Aleman-Flores, L. Alvarez-Leon, M.B. Esteban-Sanchez, R. Fuentes-Pavon, J.M. Santana-Montesdeoca, Computerized ultrasound characterization of breast tumors, International Congress Series 1281 (2005) 1063–1068.
[11] L.D. Cohen, On active contour models and balloon, CVGIP: Image Understanding 53 (2) (1991) 211–218.
[12] L.D. Cohen, I. Cohen, Finite-element methods for active contour models and balloons for 2-D and 3-D images, IEEE Transactions on Pattern Analysis and Machine Intelligence 15 (11) (1993) 1131–1147.
[13] O. Pujol, D. Gil, P. Radeva, Fundamentals of stop and go active models, Image Vision and Computing 23 (2005) 681–691.
[14] J. Tang, A multi-direction GVF snake for the segmentation of skin cancer images, Pattern Recognition 42 (2009) 1172–1179.
[15] F.Y. Shih, K. Zhang, Locating object contours in complex background using improved snakes, Computer Vision and Image Understanding 105 (2007) 93–98.
[16] I. Dagher, K.E. Tom, Waterballoons: a hybrid watershed balloon snake segmentation, Image Vision and Computing 26 (2008) 905–912.
[17] X. Zhu, P. Zhang, J. Shao, Y. Cheng, Y. Zhang, J. Bai, A snake based method for segmentation of intravascular ultrasound images and its in vivo validation, Ultrasonics 51 (2) (2011) 181–189.
[18] S.D. Fenster, J.R. Kender, Sectored snakes: evaluating learned energy segmentations, Transactions in Pattern Analysis and Machine Intelligence 23 (9) (2001) 1028–1034.
[19] M.-A. Charmi, S. Derrode, F. Ghorbel, Fourier-based geometric shape prior for snakes, Pattern Recognition Letters 29 (2008) 897–904.
[20] C. Chesnaud, Ph. Réfrégier, V. Boulet, Statistical region snake-based segmentation adapted to different physical noise models, IEEE Transactions on Pattern Analysis and Machine Intelligence 21 (11) (1999) 1145–1157.

[21] R. Ronfard, Region-based strategies for active contour models, International Journal of Computer Vision 13 (2) (1994) 229–251.
[22] S.C. Zhu, A. Yuille, Region competition: unifying snakes, region growing, and Bayes/MDL for multiband image segmentation, IEEE Transactions in Pattern Analysis and Machine Intelligence 18 (9) (1996) 884–900.
[23] T. McInerney, D. Terzopoulos, T-snakes: topology adaptive snakes, Medical Image Analysis 4 (2) (2000) 73–91.
[24] G. Giraldi, E. Strauss, A. Oliveira, Dual-T-snakes model for medical imaging segmentation, Pattern Recognition Letters 24 (2003) 993–1003.
[25] H. Delingnette, J. Montagnat, New algorithm for controlling active contours shape and topology, in: Sixth European Conference on Computer Vision (ECCV), Ireland, vol. 2, 2000, pp. 381–395.
[26] H. Delingette, J. Montagnat, Shape and topology constraints on parametric active contours, Computer Vision and Image Understanding 83 (2001) 140–171.
[27] R. Malladi, J. Sethian, B. Vemuri, Shape modeling with front propagation, IEEE Transactions in Pattern Analysis and Machine Intelligence 17 (2) (1995) 158–171.
[28] S. Osher, J.A. Sethian, Fronts propagating with curvature dependent speed: algorithms based on Hamilton–Jacobi formulation, Journal of Computational Physics 79 (1988) 12–49.
[29] V. Caselles, R. Kimmel, G. Sapiro, Geodesic active contours, International Journal of Computer Vision 22 (1) (1997) 61–79.
[30] K. Siddiqi, Y.B. Lauzière, A. Tannenbaum, S.W. Zucker, Area and length minimizing flows for shape segmentation, IEEE Transactions in Image Processing 7 (3) (1998) 433–443.
[31] X. Wang, L. He, W.G. Wee, Deformable contour method: a constrained optimization approach, International Journal of Computer Vision 59 (1) (2004) 87–108.
[32] L. He, Z. Peng, B. Everding, X. Wang, C.Y. Han, K.L. Weiss, W.G. Wee, A comparative study of deformable contour methods on medical image segmentation, Image and Vision Computing 26 (2008) 141–163.
[33] C. Xu, D. Pham, J. Prince, Image segmentation using deformable models, in: Handbook of Medical Imaging, Medical Image Processing and Analysis, vol. 2, SPIE Press, 2000, pp. 129–174.
[34] C. Li, J. Liu, M.D. Fox, Segmentation of external force field for automatic initialization and splitting of snakes, Pattern Recognition 38 (11) (2005) 1947–1960.
[35] M. Rochery, I.H. Jermyn, J. Zerubia, Higher order active contours, International Journal of Computer Vision 69 (1) (2006) 27–42.
[36] C. Xu, J.L. Prince, Snakes, shapes, and gradient vector flow, IEEE Transaction on Image Processing 7 (3) (1998) 359–369.
[37] C. Xu, J.L. Prince, Gradient vector flow: a new external force for snakes, Proceedings of the International IEEE Computer Society Conference on Computer Vision and, Pattern Recognition (1997) 66–71.
[38] C. Xu, J.L. Prince, Generalized gradient vector flow external forces for active contours, Signal Processing 71 (2) (1998) 131–139.
[39] M. Wei, Y. Zhou, M. Wan, A fast snake model based on non-linear diffusion for medical image segmentation, Computerized Medical Imaging and Graphics 28 (3) (2004) 109–117.
[40] J. Mille, Narrow band region-based active contours and surfaces for 2d and 3d segmentation, Computer Vision and Image Understanding 113 (2009) 946–965.
[41] Y. Shang, X. Yang, L. Zhu, R. Deklerck, E. Nyssen, Region competition based active contour for medical object extraction, Computerized Medical Imaging and Graphics 32 (2) (2008) 109–117.
[42] A.K. Jumaat, W.E.Z.W.A. Rahman, A. Ibrahim, R. Mahmud, Segmentation of masses from breast ultrasound images using parametric active contour algorithm, Procedia – Social and Behavioral Sciences 8 (2010) 640–647.
[43] D. Chen, R. Chang, W. Wu, W. Moon, W. Wu, 3-D breast ultrasound segmentation using active contour model, Ultrasound in Medicine and Biology 29 (7) (2003) 1017–1026.
[44] R.-F. Chang, W.-J. Wu, W.K. Moon, W.-M. Chen, W. Lee, D.-R. Chen, Segmentation of breast tumor in three-dimensional ultrasound images using three-dimensional discrete active contour model, Ultrasound in Medicine and Biology 29 (11) (2003) 1571–1581.
[45] T. McInerney, Sketch-snakes: sketch-line initialized snakes for efficient interactive medical image segmentation, Computerized Medical Imaging and Graphics 32 (5) (2008) 331–352.
[46] G. Hamarneh, T. Gustavsson, Combining snakes and active shape models for segmenting the human left ventricle in echocardiographic images, Computers in Cardiology (2000) 115–118.
[47] C.M. Chen, H.H.S. Lu, Y.C. Lin, An early vision-based snake model for ultrasound image segmentation, Ultrasound in Medicine and Biology 26 (2) (2000) 273–285.
[48] M. Mignotte, J. Meunier, A multiscale optimization approach for the dynamic contour-based boundary detection issue, Computerized Medical Imaging and Graphics 25 (3) (2001) 265–275.
[49] A. Rodtook, S.S. Makhanov, Continuous force field analysis for generalized gradient vector flow field, Pattern Recognition 43 (10) (2010) 3522–3538.
[50] H.D. Cheng, J. Shan, W. Ju, Y. Guo, L. Zhang, Automated breast cancer detection and classification using ultrasound images: a survey, Pattern Recognition 43 (1) (2010) 299–317.
[51] J.S. Lee, Digital image enhancement and noise filtering by using local statistics, IEEE Transactions in Pattern Analysis and, Machine Intelligence PAM1-2 (1980) 165–168.
[52] V.S. Frost, J.A. Stiles, K.S. Shanmugan, J.C. Holtzman, A model for radar images and its application to adaptive digital filtering of multiplicative noise, IEEE Transactions on Pattern Analysis and Machine Intelligence PAMI-4 (1982) 157–165.
[53] D.T. Kuan, A.A. Sawchuk, T.C. Strand, P. Chavel, Adaptive restoration of images with speckle, IEEE on Transactions Acoustic, Speech and, Signal Processing ASSP-35 (1987) 373–383.
[54] S. Gupta, L. Kaur, R.C. Chauhan, S.C. Saxena, A versatile technique for visual enhancement of medical ultrasound images, Digital Signal Processing 17 (2007) 542–560.
[55] Y. Zhang, R. Sankar, W. Qian, Boundary delineation in transrectal ultrasound image for prostate cancer, Computers in Biology and Medicine 37 (2007) 1591–1599.
[56] B. Liu, H.D. Cheng, J. Huang, J. Tian, X. Tang, J. Liu, Probability density difference-based active contour for ultrasound image segmentation, Pattern Recognition 43 (2010) 2028–2042.
[57] P. Perona, J. Malik, Scale-space and edge detection using anisotropic diffusion, IEEE Transactions on Pattern Analysis and Machine Intelligence 12 (1990) 629–639.
[58] R.N. Czerwinski, D.L. Jones, W.D. O'Brien, Detection of lines and boundaries in speckle images – application to medical ultrasound, IEEE Transactions on Medical Imaging 18 (1999) 126–136.
[59] A. Lopes, R. Touzi, E. Nezry, Adaptive speckle filters and scene heterogeneity, IEEE Transactions on Geoscience and Remote Sensing 28 (1990) 992–1000.
[60] Y.-L. Huang, Y.-R. Jiang, D.-R. Chen, W.K. Moon, Level set contouring for breast tumor in sonography, Journal of Digital Imaging 20 (3) (2007) 238–247.
[61] B. Levienaise-Obadia, A.H. Gee, Adaptive segmentation of ultrasound images, Image Vision and Computing 17 (8) (1999) 583–588.
[62] J. Yu, J. Tan, Object density-based image segmentation and its applications in biomedical image analysis, Computer Methods and Programs in Biomedicine 96 (2009) 193–204.
[63] L. Vincent, Morphological grayscale reconstruction in image analysis Applications and efficient algorithms, IEEE Transactions on Image Processing 2 (1993) 176–201.
[64] M. Mignotte, J. Meunier, A multiscale optimization approach for the dynamic contour-based boundary detection issue, Computerized Medical Imaging and Graphics 25 (2001) 265–275.
[65] N. Ray, B. Chanda, J. Das, A fast and flexible multiresolution snake with a definite termination criterion, Pattern Recognition 34 (2001) 1483–1490.
[66] S. Chucherd, A. Rodtook, S.S. Makhanov, Phase portrait analysis for multiresolution generalized gradient vector flow, IEICE Transactions on Information and Systems E93-D (10) (2010) 2822–2835.
[67] F.N. Fritsch, R.E. Carlson, Monotone piecewise cubic interpolation, SIAM Journal of Numerical Analysis 17 (1980) 238–246.
[68] K.R. Castelmen, Digital Image Processing, Prentice Hall, 1996.
[69] H. Chipman, R. Tibshirani, Hybrid hierarchical clustering with applications to microarray data, Biostatistics 2 (7) (2006) 286–301.
[70] G. Naldi, L. Pareschi, G. Toscani, Relaxation schemes for PDEs and applications to fourth order diffusion equations, Surveys on Mathematics for Industry 10 (2002) 315–343.
[71] C.Y. Hsu, C.Y. Liu, C.M. Chen, Automatic segmentation of liver PET images, Computerized Medical Imaging and Graphics 32 (2008) 601–610.
[72] C.Y. Hsu, S.H. Chen, K.L. Wang, Active contour model with a novel image force field, in: Proceeding of the Conference CVGIP-2003, Taiwan, 2003, pp. 477–483.
[73] C.Y. Hsu, K.F. Wang, H.C. Wang, K.K. Tseng, Automatic extraction of face contours in images and videos, Future Generation Computer Systems 28 (2012) 322–335.
[74] O. Ghita, P.F. Whelan, A new GVF-based image enhancement formulation for use in the presence of mixed noise, Pattern Recognition 43 (2010) 2646–2658.
[75] B. Li, S.T. Acton, Active contour external force using vector field convolution for image Segmentation, IEEE Transactions on Inage Processing 16 (8) (2007) 2096–2106.
[76] H. Park, T. Schoepflin, Y. Kim, Active contour model with gradient directional information: Directional snake, IEEE Transactions in Circuits and Systems for Video Technology 11 (2) (2001) 252–256.
[77] J. Cheng, S.W. Foo, Dynamic directional gradient vector flow for snakes, IEEE Transactions on Image Processing 15 (6) (2006) 1563–1571.
[78] M.-P. Dubuisson, A.K. Jain, A modified Hausdorff distance for object matching proceedings, in: International Conference on Pattern Recognition, Israel, 1994, pp. 566–568.
[79] D. Mumford, J. Shah, Optimal approximation by piecewise smooth functions and associated variational problems, Communications on Pure Applied Mathematics 42 (1989) 577–685.
[80] A. Vitti, The Mumford–Shah variational model for image segmentation: an overview of the theory, implementation and use, ISPRS Journal of Photogrammetry and Remote Sensing 69 (2012) 50–64.
[81] L. Vese, T.F. Chan, A multiphase level set framework for image segmentation using the Mumford and Shah model, International Journal of Computer Vision 50 (3) (2002) 271–293.
[82] Y. Yuan, C. He, Adaptive active contours without edges, Mathematical and Computer Modeling 55 (2012) 1705–1721.

[83] L. Chan-Fei1, W. Yao-Nanm, L. Guo-Cai, A new splitting active contour framework based on Chan–Vese piecewise smooth model, Acta Automatica Sinica 34 (6) (2008) 660–664.
[84] E.H.S. Diop, V. Burdin, Bi-planar image segmentation based on variational geometrical active contours with shape priors, Medical Image Analysis 17 (2013) 165–181.
[85] A.K. Jain, Y. Zhong, S. Lakshmanan, Object matching using deformable templates, IEEE Transactions on Pattern Analysis and Machine Intelligence 18 (3) (1996) 267–278.
[86] <http://www.queensirikitcentreforbreastcancer.com/en/our_team.php>.